Carbon Capture Science & Technology 5 (2022) 100068

Contents lists available at ScienceDirect

Carbon Capture Science & Technology

journal homepage: www.elsevier.com/locate/ccst

Full Length Article

Visualising coke-induced degradation of catalysts used for CO_2-reforming of methane with X-ray nano-computed tomography

Rhodri E. Owen[a,b], Ye Shui Zhang[a,b], Tobias P. Neville[a], George Manos[a], Paul R Shearing[a,b], Dan J.L. Brett[a,b], Josh J. Bailey[a,c,*]

[a] Electrochemical Innovation Lab, Department of Chemical Engineering, UCL, London WC1E 7JE, UK
[b] Quad One, Becquerel Avenue, Harwell Science and Innovation Campus, The Faraday Institute, Didcot OX11 0RA, UK
[c] School of Mechanical and Aerospace Engineering, Queen's University Belfast, Belfast BT9 5AH, UK

ARTICLE INFO

Keywords:
CO_2-reforming
Coking
Bimetallic Catalysts
Cracking
X-ray nano-CT

ABSTRACT

The switch from a carbon-based to a hydrogen-based economy requires environmentally friendly methods for hydrogen production. CO_2-reforming of methane promises to be a greener alternative to steam-methane reforming, which accounts for the majority of hydrogen production today. For this dry process to become industrially competitive, challenges such as catalyst deactivation and degradation through coke formation must be better understood and ultimately overcome. While bulk characterisation methods provide a wealth of useful information about the carbon formed during coking, spatially resolved techniques are required to understand the type and extent of degradation of supported catalyst particles themselves under coking conditions. Here, lab-based X-ray nano-computed tomography, in conjunction with a range of complementary techniques, is utilised to understand the effects of the nickel-to-cobalt ratio on the degradation of individual supported catalyst particles. Findings suggest that a bimetallic system greatly outperforms monometallic catalysts, with the ratio between nickel and cobalt having a significant impact on the type and quantity of the carbon formed and on the extent of supported catalyst breakdown.

1. Introduction

With accelerating climate change and a dependence on dwindling supplies of non-renewable carbonaceous energy resources, much research is focused on lowering greenhouse gas emissions as well as switching from a carbon-based to a hydrogen-based economy (Oliveira et al., 2021). Currently the majority of hydrogen is produced from steam-methane reforming (SMR), a non-sustainable and polluting process (Bauer et al., 2022). While attempts are being made to improve sustainability through the sequestration of the produced CO_2 to provide so-called blue hydrogen, realistically, this is not sufficiently sustainable (Bauer et al., 2022). Another alternative which has been gaining increasing attention (Jang et al., 2019) as a potentially more environmentally friendly method of production, is the dry reforming of methane (DRM) (Lavoie, 2014). The DRM process replaces the water used in SMR with second greenhouse gas, carbon dioxide (Eq. (1)).

$$CH_4 + CO_2 \rightarrow 2CO + 2H_2 \Delta H^o = +247.3\,\mathrm{kJ\,mol^{-1}} \quad (1)$$

CO_2 and CH_4 are the chief contributors to the greenhouse effect and as such, methods that convert both of these gases into other more environmentally benign products are key to reducing global greenhouse gas emissions. As a highly endothermic reaction, typical operating temperatures for DRM of over 600 °C are implemented to boost conversion, though catalysts are still required to achieve commercially viable reaction rates. Noble metal catalysts have shown high DRM activity with good stability (Edwards and Maitra, 1995), however their high cost prohibits their implementation as the sole active catalytic species (Pakhare and Spivey, 2014). More recently, focus has shifted towards cheaper, more abundant, transition-metal-based catalysts in an attempt to achieve a cost-effective process. Of the metals investigated thus far, nickel-based catalysts, supported on inorganic oxides, represent one of the most industrially relevant choices, due to their low cost, good activity, and the relatively high abundance of nickel (Kawi et al., 2015).

Despite their high activity for DRM, nickel catalysts still present issues that must be overcome before they are utilised more widely. The main issue at present is rapid catalyst deactivation through metal sintering and degradation through coking (Kim et al., 2007). Coking refers to the deposition of carbon on the surface of the catalyst, mainly through unwanted side reactions such as the disproportionation of the carbon monoxide product, the Boudouard reaction (Eq. (2)), and the cracking of methane (Eq. (3)). The formation of coke through these reactions is

* Corresponding author at: Electrochemical Innovation Lab, Department of Chemical Engineering, UCL, London WC1E 7JE, UK.
E-mail address: j.bailey@qub.ac.uk (J.J. Bailey).

https://doi.org/10.1016/j.ccst.2022.100068
Received 30 June 2022; Received in revised form 24 August 2022; Accepted 7 September 2022

more serious for DRM than SMR due to the higher CH_4:CO_2 ratio and lack of the oxidising steam component which helps to prevent carbon build-up.

$$2CO \rightarrow C + CO_2 \Delta H^o = +75\,kJ\,mol^{-1} \quad (2)$$

$$CH_4 \rightarrow C + 2H_2 \Delta H^o = -172\,kJ\,mol^{-1} \quad (3)$$

The formation of carbon can block catalyst pores and coat its active sites, resulting in a decrease in catalytic activity. The type and quantity of coke formed is dependant on the reaction conditions, such as the ratio of reactants, the temperature and the nature of the catalyst employed. At the relatively high temperatures employed in DRM, the formation of coke through the cracking of methane (Eq. (3)) is reported to be the main reaction responsible for coke formation (Liu et al., 2011).

As aforementioned, a typical supported catalyst used for this transformation is composed of metallic nickel supported on an inorganic oxide, such as alumina. Catalysts of this nature have thus far, however, proven too prone to coke formation (Liu et al., 2011; He et al., 2021; Swaan et al., 1994). Much current work focuses on the optimisation of this catalyst system to reduce coke formation while retaining the desired high activity (Wang et al., 2018). The addition of promoters such as noble metals and rare earth elements has proven successful in reducing the extent of coking during the DRM (Laosiripojana et al., 2005; Tsyganok et al., 2005). The support used can also play an important role in producing catalysts with improved resistance to coke deposition (Luisetto et al., 2012; Gadalla and Sommer, 1988; Erdogan et al., 2018). In addition to the composition of the utilised catalyst, the preparation method has also been demonstrated to have an effect on the nature of coke formation(Abdollahifar et al., 2016).

An important area of research is now the use of bimetallic catalysts for reduced carbon deposition (Sasson Bitters et al., 2022; Bian et al., 2017; Yentekakis et al., 2021). The chemical and physical properties of bimetallic catalysts differ from the properties of either of the metals when used in isolation and as such the combination can offer systems with higher catalyst activities and less coking than is achievable with monometallic catalysts. Co-metals studied in conjunction with nickel include cobalt, copper, iron, chromium, and bismuth, amongst many others (Sasson Bitters et al., 2022; Han et al., 2021; Sharifi et al., 2014; Li et al., 2019; Rouibah et al., 2017; Sutthiumporn et al., 2012). Of these, cobalt has generated some of the most significant interest as a potential co-metal for both improved catalyst activity and resistance to coking (Sasson Bitters et al., 2022).

The addition of a small amount of cobalt to a nickel system is sufficient to enhance both the catalytic performance and improve resistance to coking, however, due to cobalt's lower activity relative to nickel, the addition of too much can be detrimental to performance. As such, the ratio of cobalt to nickel in a system can have a significant effect on catalytic activity (Sengupta et al., 2014; Li et al., 2022). Understanding how this nickel-to-cobalt ratio effects the composition and quantity of the coke formed is less explored, although in general it has been observed that higher quantities of cobalt result in less carbon formation (Takanabe et al., 2005). Despite a higher resistance to coking being observed in nickel-cobalt bimetallic catalysts, carbon formation still occurs and is unlikely to be eliminated as an issue entirely. Therefore, to develop catalyst systems that are stable for the long durations required for industrial applications, a better understanding of coke formation in this process is required to aid appropriate catalyst design.

Characterisation of coke, understanding its formation and its effect on catalyst degradation is still a challenging process since carbon formation and its consequences on catalyst performance and durability occur across multiple time and length scales. Several characterisation techniques have proven vital in understanding the bulk properties of the coke formed, such as Raman spectroscopy and thermogravimetric analysis (TGA) (Sasson Bitters et al., 2022). While these techniques can provide important information about the bulk properties and quantity of carbon formed, they provide little insight into how this carbon formation affects individual catalyst particles and no spatial information as to where coke formation occurs.

More recently, tomographic studies of catalytic systems have begun to be reported and can provide information about catalyst structure, performance and degradation that is not available through bulk techniques (Beale et al., 2014; Meirer and Weckhuysen, 2018). Studies have shown that these tomographic techniques are useful for understanding the porosity in fluidised catalytic cracking (FCC) catalysts (Meirer et al., 2015; Dasilva et al., 2015; Bare et al., 2014) as well as their degradation after use, including structural changes and the redistribution of elements (Meirer et al., 2015; Gambino et al., 2020). A limited number of studies have investigated coke formation on FCC catalysts with a focus on its position and effect on porosity (Veselý et al., 2021; Zhang et al., 2020). Similar techniques have also been applied to other catalyst systems such as those used for the Fischer-Tropsch process (Cats et al., 2016; Price et al., 2017) and in automotive applications (Schmidt et al., 2017). Recently hard X-ray ptychographic computed tomography was conducted using synchrotron radiation to investigate the structure of Ni/Al_2O_3 DRM catalysts (Weber et al., 2020) and the deposition of coke (Weber et al., 2021). Using this technique, Weber and co-workers were able to visualise the three-dimensional position of the formed coke throughout a single catalyst particle.

Since catalyst properties influence the quantity, type and location of coke and have long-term implications on the catalyst performance and structural stability, we report here an investigation into the effect of the nickel-to-cobalt ratio on coke formation in $Ni/Co/Al_2O_3$ catalysts. The properties and quantities of coke formed are reported alongside easily accessible, lab-based X-ray nano-computed tomography data which gives spatially resolved information about coke formation on individual catalyst particles and new insights into catalyst degradation pathways after extensive coking, as a function of the nickel-to-cobalt ratio.

Table 1
Calculated nickel, cobalt and alumina quantities in the prepared catalysts and their nomenclature.

Nomenclature	Ni Content (wt%)	Co Content (wt%)	Al_2O_3 Content (wt%)
20Ni	20	0	80
15Ni5Co	15	5	80
10Ni10Co	10	10	80
5Ni15Co	5	15	80
20Co	0	20	80

2. Experimental

2.1. Catalyst preparation

A range of catalysts containing various ratios of nickel and cobalt were prepared using incipient wetness impregnation. Table 1 shows the nominal nickel, cobalt and alumina content of the prepared catalysts based on fully reduced, metallic nickel and cobalt. EDX measurements were conducted to verify these values which showed broad agreement with the trend expected from calculated loadings. Particle-to-particle variation was observed; the discrepancy between nominal and measured values is thought to be due to the small number of particles available for measuring using this approach. Various quantities of aqueous solutions of $Ni(NO_3)_2{\bullet}6H_2O$ (99.98% metal basis, Sigma Aldrich) and $Co(NO_3)_2{\bullet}6H_2O$ (≥98%, Sigma Aldrich) were slowly added to γ-alumina, 50–200 μm, 60 Å pore size (Acros Organics). The quantity of each metal precursor was calculated to give the values shown in Table 1 when fully reduced. The mixtures of alumina and metal precursors were dried in an oven at 100 °C for 4 h. The resulting dried powder was then calcined in static air at 550 °C for 16 h and allowed to slowly cool to room temperature inside a baffle furnace.

2.2. Catalyst characterisation

2.2.1. pXRD

Powder X-ray diffraction (pXRD) of the as-calcined, as-reduced, and coked samples was performed on a SmartLab diffractometer (Rigaku, Japan) fitted with a Mo K_α (λ = 0.71 Å) source. Samples were scanned from 2Θ = 5° to 80° with a step size of 0.01° and a step time of 0.6°.min^{-1}. Peak identification and data analysis were conducted using SmartLab Studio II Software v4.1.0.182 (Rigaku, Japan) and the Crystallography Open Database (Gražulis et al., 2012).

2.2.2. TGA

The carbon deposited on each sample was analysed using a PerkinElmer Pyris 1 (PerkinElmer, US) thermogravimetric analyser. Approximately 4–8 mg of each coked catalyst was placed in a platinum sample crucible and heated to 900 °C with a ramp rate of 10 °C.min^{-1} under an air flow rate of 20 mL.min^{-1}.

2.2.3. Raman spectroscopy

Raman spectra of the as-reduced and coked samples was acquired using a Renishaw Invia Raman (Renishaw, UK) microscope with a RL532C class 3B continuous wave, diode-pumped solid-state laser which operates at 532 nm. Data was obtained over a period of 30 s at low laser power (< 15 mW), averaging over five acquisitions taken between 1000 and 1800 cm^{-1}. Data was collected at five separate points on different catalyst particles to ensure the results were representative of the bulk sample. Data fitting was conducted using OriginPro 2021b data analysis and graphing software (OriginLab Corporation, U.S.A.) according to the method reported by Sadezky et al. (2005).

2.2.4. TEM

Transmission electron microscopy (TEM) was conducted using a JEOL 2100 LaB_6 transmission electron microscope (JEOL, Japan). Samples were prepared by sonicating in ethanol before dropping the suspension onto carbon-coated copper discs.

2.2.5. pSEM

Powder scanning electron microscopy (pSEM) of the as-calcined, as-reduced, and coked samples was conducted on a Zeiss SEM EVO MA10 (Carl Zeiss, Germany) by loading the respective powders on conventional sticky carbon tabs atop aluminium stubs and coating with nanometre-thick layers of gold using a Quorum SC7620 Mini Sputter Coater (Quorum, UK) to avoid charging. Micrographs were taken at various magnifications to capture general morphology, cracking extent, and the carbon formed on coked samples.

2.2.6. xsSEM/EDX

Cross-sectional scanning electron microscopy (xsSEM) and energy-dispersive X-ray spectroscopy (EDX) were performed on the same instrument as pSEM with the use of an INCA x-act SDD detector and INCA suite V5.05 software (Oxford Instruments, UK). For the 20Ni, 10Ni10Co and 20Co samples, as calcined powders were encased in an epoxy puck by overnight vacuum-curing of a mixture of epoxy resin and hardener (EpoFix kit, Struers, Denmark) before grinding with increasingly fine silicon carbide papers (Buehler, US). The epoxy pucks were subsequently carbon coated to prevent charging. This allowed for mapping of the metal distribution within the catalyst particles.

2.2.7. X-ray nano-CT

Lab-based X-ray nano-computed tomography (nano-CT) was performed for both the reduced and coked variants of the 20Ni, 10Ni10Co, and 20Co samples, using a Zeiss Xradia 810 Ultra (Carl Zeiss) with a fixed X-ray energy of 5.4 keV and field-of-view of 65 × 65 µm. Imaging was performed with either binning 1 (voxel dimension of approximately 63 nm) or binning 2 (voxel dimension of approximately 126 nm) in both absorption and phase contrast modes. The full set of parameters are given in Table 2.

Reconstruction of all scans was performed in Zeiss XMReconstructor software utilising a standard filtered back-projection algorithm. Absorption and phase contrast tomograms were combined for all but the 20Ni coked sample (due to imperfect registration of the two tomograms) using the Zeiss DSCoVer tool (Version 16.1) before data processing and visualisation were carried out in Avizo 2022.1 (Thermo Fisher Scientific, US). All tomograms were Gaussian-filtered (3D, standard deviation of 1.1) and imported into open-source, machine-learning segmentation software (Ilastik 1.3.3 (Berg et al., 2019)) whereupon manual training was provided for the central slice and an initial segmentation prediction was generated. This approach (shown in Fig. S1) was taken as traditional supervised segmentation approaches in Avizo, such as watershed segmentation, did not appear to generate a reliable result. From the overlay of this prediction on the raw data, manual corrections were made by training two more slices before the final segmentation output was generated. Raw and segmented orthoslices and volume renderings were output from Avizo and equally sized sub-volumes (of *ca.* 6600 µm^3) were extracted from each segmented tomogram before applying voxel counting to assess the phase fractions for solids and pores. The spatial resolution in each tomogram was estimated by using a sharp-edge fitting (Fig. S2). This involved drawing line plots across sharp feature boundaries and the number of voxels required to move from 10% to 90% of the voxel intensity difference between the feature and the background was combined with the nominal voxel size to provide an estimate of the true spatial resolution in each acquired tomogram (See Table 3 for estimated spatial resolution). Small particles, meso- and micropores below these resolution limits will not be detected and only features at or above will appear detectable in the acquired images.

2.3. Catalyst pre-treatment and accelerated coking tests

Catalyst pre-treatment and accelerated coking tests were conducted in a tube furnace (Lenton, UK). Catalysts were held within a quartz tube with gas flow of nitrogen, hydrogen and methane controlled using EL-Flow mass flow controllers (Bronkhorst, Germany). For catalyst pre-treatment, the sample under test was heated at 20 °C.min^{-1} to 700 °C under a flow of 100 sccm N_2. Once at temperature, a flow of 100 sccm 4% H_2 in N_2 was introduced and maintained for 2 h. To understand the long-term effects of coking on catalysts for CO_2 reforming of methane, accelerated coking tests were conducted. These tests involved inducing high levels of coking by using only methane as a feed gas as is commonly done for *in situ* experiments (Weber et al., 2021; Mutz et al., 2018). The catalyst samples under test were heated to 600 °C under a flow of 100 sccm N_2. Once at temperature, a mixture of 5% CH_4 in N_2 was introduced at 100 sccm. The accelerated coking tests were conducted over a period of 4 h and once complete the gas flow was switched back to 100 sccm N_2 and the sample allowed to cool naturally.

3. Results and discussion

3.1. Catalyst characterisation

To study the effect of nickel-to-cobalt ratio on the quantity and properties of the carbon formed during accelerated coking tests, a range of catalysts were prepared according to the procedure outlined in Section 2.1 and hereafter will be referred to by the nomenclature shown in Table 1. Representative SEM micrographs of each catalyst composition in the as-calcined state are shown in Fig. 1 (a-f). Each of the catalysts were observed to be similar in morphology with particle sizes remaining relatively consistent across all compositions. Some surface roughness was observed in each of the samples, potentially related to the nickel and/or cobalt metal oxide loaded onto the support. Some evidence of support particle cracking was also observed and, although minimal and difficult to observe in the 20Ni and 20Co samples, this was

Table 2
X-ray nano-CT parameters for all acquired tomograms in this study.

Sample	Type	Mode	Exposure time (s)	Projections	Binning	Voxel size (nm)
20Ni	Reduced	Absorption	32	1101	1	63
		Phase	32	1101	2	126
	Coked	Absorption	24	1001	1	63
		Phase	48	1001	1	63
10Ni10Co	Reduced	Absorption	24	1101	1	63
		Phase	36	1101	2	126
	Coked	Absorption	14	1101	1	63
		Phase	56	1101	1	63
20Co	Reduced	Absorption	32	1101	1	63
		Phase	42	1101	2	126
	Coked	Absorption	12	1101	1	63
		Phase	48	1101	1	63

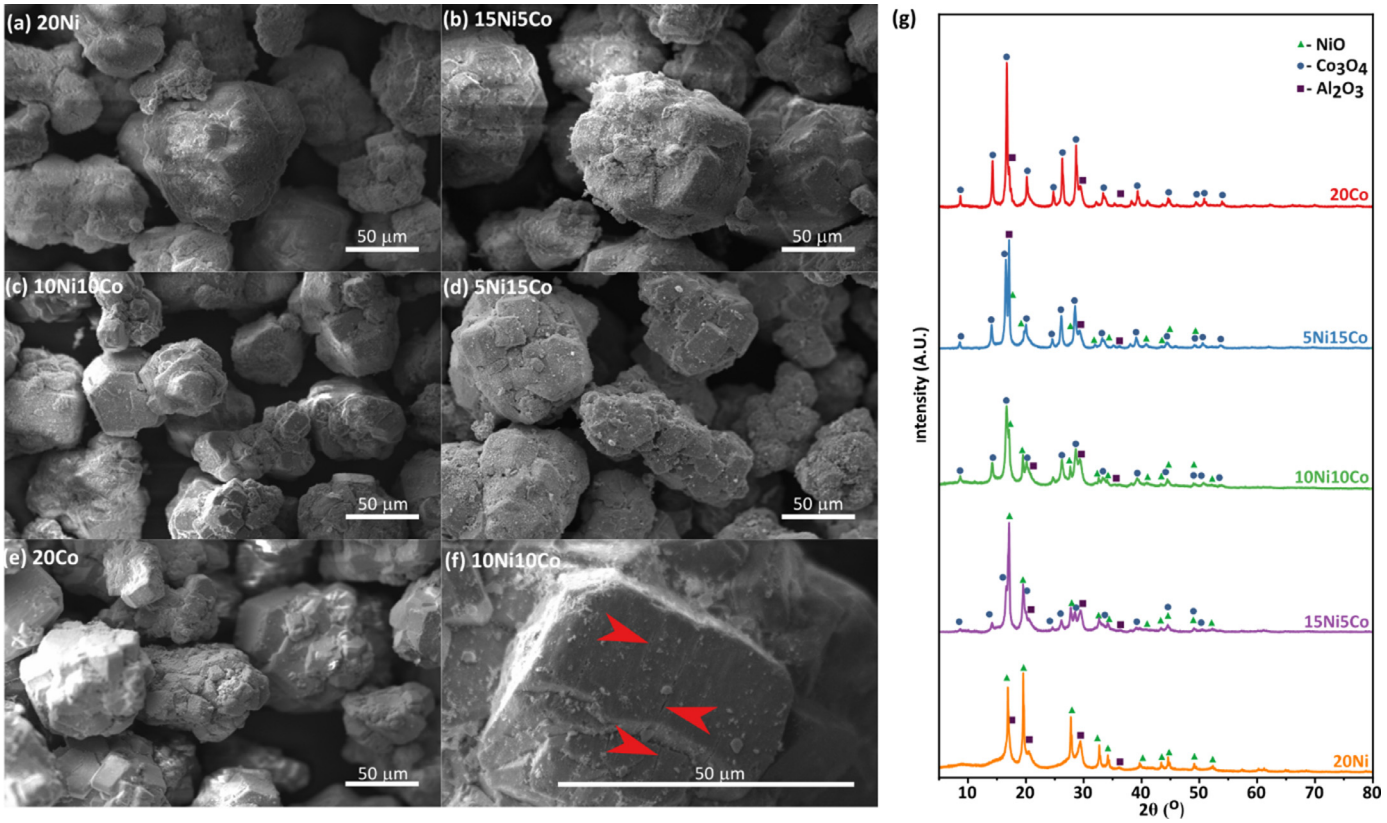

Fig. 1. Representative SEM micrographs of the as-calcined catalysts: (a) 20Ni; (b) 15Ni5Co; (c) 10Ni10Co; (d) 5Ni15Co; and (e) 20Co. (f) A higher magnification micrograph of a 10Ni10Co catalyst particle, illustrating the presence of small cracks after calcination, cracks are highlighted by red arrows. (g) pXRD patterns recorded for the as-calcined catalysts.

Table 3
The estimated spatial resolution of the X-ray CT measurements in this study.

State	Sample	Estimated Spatial Resolution (nm)
Reduced	20Ni	740
	10Ni10Co	660
	20Co	500
Coked	20Ni	630
	10Ni10Co	320
	20Co	390

more clearly observed in the catalysts containing mixtures of the two metals. An SEM image of 10Ni10Co at higher magnification is shown in Fig. 1(f); here a small number of cracks appeared to be running parallel to one another, suggesting a slight delamination in a particular crystallographic direction. pXRD analysis performed on the as-calcined catalysts, displayed in Fig. 1(g), shows that the monometallic samples (20Ni and 20Co) consisted primarily of their respective oxide and the alumina support. A small unidentified peak ($2\theta = 17.1^{\circ}$), potentially indicating a minor impurity, is present in all samples. The fact that this is observed in an XRD pattern of the as-received alumina source (see Fig. S3) suggests that this is the source; since it is present in all samples it is unlikely to affect the results of these studies. For the bimetallic cases (15Ni5Co, 10Ni10Co and 5Ni15Co), all three phases, γ-Al_2O_3, NiO, and Co_3O_4 are evident, with no indication of any residual nitrates. Despite overlapping peaks, there is some evidence of the formation of some $NiAl_2O_4$, which is common for catalysts calcined at these temperatures (Siang et al., 2018). There is some evidence that this phase can improve nickel dispersion and reduce nanoparticle size, improving catalytic activity (He et al., 2021). The presence of this spinel structure is important since this phase has been shown to be more tolerant to

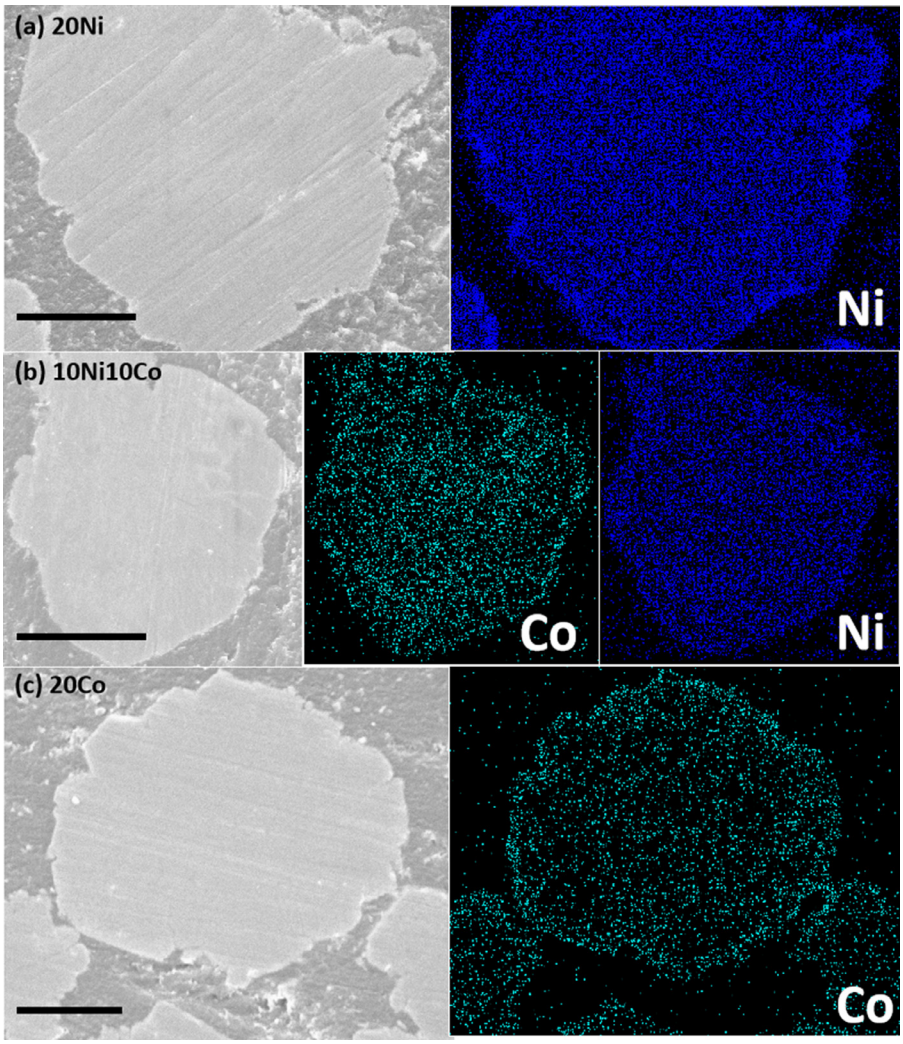

Fig. 2. Cross-sectional SEM (xsSEM) and energy-dispersive X-ray (EDX) spectroscopic mapping, illustrating the Ni and Co distribution for (a) 20Ni; (b) 10Ni10Co; and (c) 20Co samples. Scale bar = 25 μm.

coking and less likely to sinter (Salhi et al., 2011). Based on the XRD patterns, there is still a significant quantity of NiO present in the sample which will be more readily reduced and will likely contribute more significantly to the coking behaviour of the catalysts.

The majority of metals present in the catalyst are expected to be present as nanoparticles throughout the internal microporous structure of the alumina support. To investigate the distribution of nickel and cobalt in the alumina support particle, xsSEM/EDX measurements were taken on 20Ni, 10Ni10Co, and 20Co. These tests involved encasing the catalyst powder in an epoxy resin before grinding with silicon carbide abrasives allowing for SEM and EDX measurements to be conducted on a smooth cross-section of each of the particles. The results from these tests are displayed in Fig. 2. The 20Ni and 20Co particles investigated showed a uniform distribution of each of the metals throughout the particle, indicating thorough impregnation of the precursor salts throughout the alumina support. The bimetallic 10Ni10Co sample showed a similar, even distribution throughout the particle, again indicating appropriate impregnation and effective mixing of cobalt and nickel with no major agglomeration of either metal in any area.

3.2. Catalyst pre-treatment

Prior to use, the catalysts analysed in Section 3.1 were first reduced to form metallic nickel and cobalt. This reduction step was achieved by heating the as-calcined samples at 700 °C and flowing 4% H_2 in N_2 over each sample for 2 h. Since this reduced form is the active phase of the catalyst, analysis of these resulting powders was also conducted to determine any changes that may have occurred during this short, high-temperature treatment. Representative SEM micrographs of each of the reduced catalysts are shown in Fig. 3. No significant change in catalyst morphology was observed, with the individual catalyst particles remaining similar in both size and morphology to the as-calcined samples shown in Fig. 1. No significant change in cracking or crack sizes was observed, indicating that short-term exposure to a high temperature reducing environment does not result in significant catalyst particle cracking.

Higher magnification images of selected catalysts are shown in Fig. 3 (f-i), where slight changes in morphology of some of the smaller particles on the catalyst surface were observed, suggesting that while the majority of the metals are well dispersed throughout the support particle, some small micron-scale deposits may be present on the outer surface of each particle, somewhat agglomerated by the reduction procedure.

After reduction at 700 °C for 2 h in an atmosphere of 4% H_2 in N_2, pXRD analysis was performed on the complete set of as-reduced catalysts, X-ray diffraction patterns of which are shown in Figs. S4-8. As expected, a characteristic new Ni^0 peak appeared at $2\theta = 23.2^\circ$ in the reduced 20Ni sample and equally, characteristic NiO peaks at $2\theta = 19.6^\circ$, 27.8° were no longer present, consistent with the full reduction of any nickel oxides present. In the reduced 20Co case, a characteristic new Co^0 peak appeared at $2\theta = 23.1^\circ$, however, some characteristic Co_3O_4 peaks at $2\theta = 16.7^\circ$, 28.7° persisted, albeit at a lower intensity. This

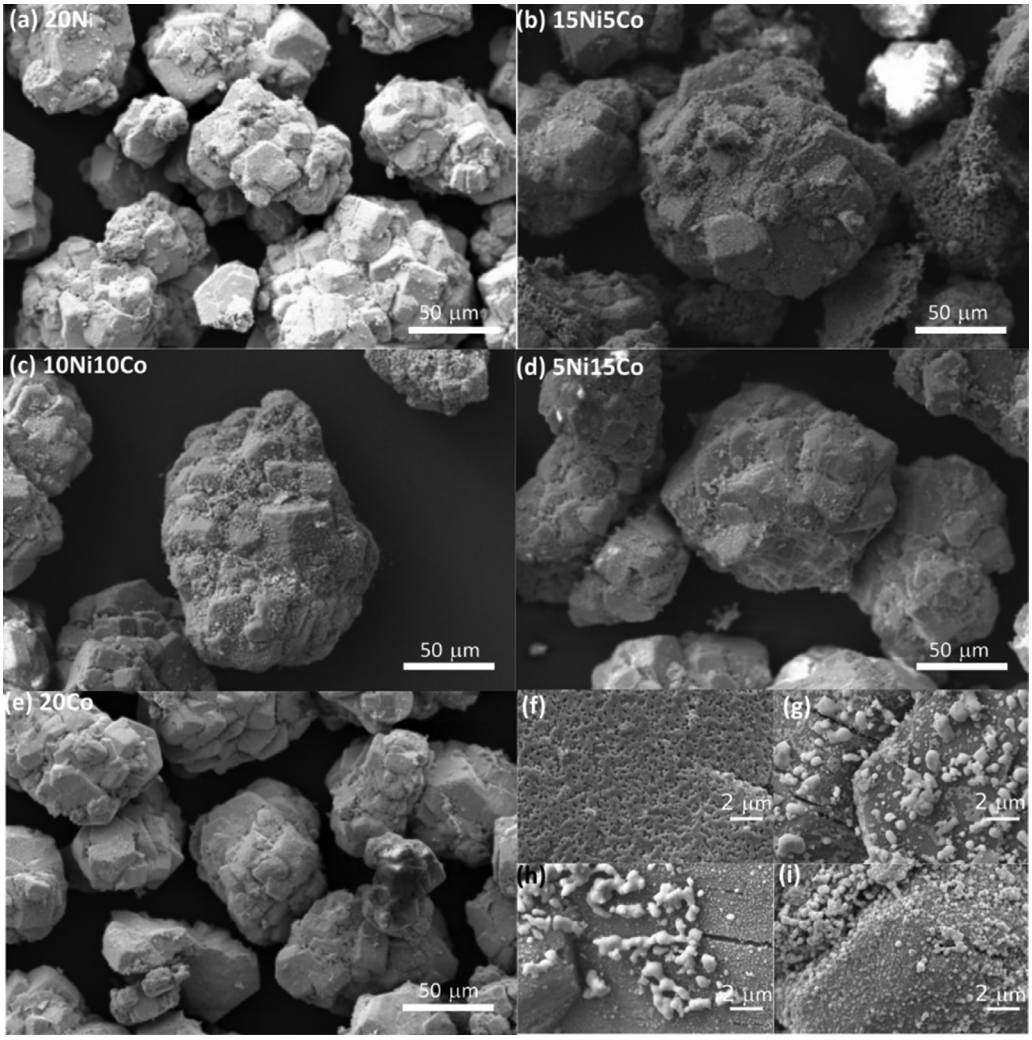

Fig. 3. SEM micrographs of as-reduced catalysts: (a) 20Ni; (b) 15Ni5Co; (c) 10Ni10Co; (d) 5Ni15Co; (e) 20Co; (f-i) Higher magnification SEM micrographs of (f) 20Ni; (g)15Ni5; (h) 10Ni10Co; and (i) 20Co, showing agglomeration of excess metal on the support surface.

indicated that some residual oxide remained present after the reduction step, although it is not clear if this residual oxide is present due to incomplete reduction of the nickel oxide, or due to a small degree of re-oxidation after reduction, prior to XRD measurements. In the bimetallic cases (15Ni5Co, 10Ni10Co and 5Ni15Co), there was evidence of γ-Al_2O_3 as well as characteristic peaks for both metals (Ni and Co), and as with the pure Co sample, there was still some evidence of small quantities of residual Co_3O_4. Testing showed that while small quantities of residual Co_3O_4 remain at this temperature (700 ˚C), the majority of the oxides are reduced.

3.3. Accelerated coking tests

Industrial catalysts are subjected to use online for thousands of hours to make processes cost effective. As such, for the bimetallic Ni/Co catalysts to be developed commercially, thorough understanding of the effects of long-term coking are required. Most papers that cover the coking of Ni/Co catalysts tend to only test catalysts for hours to occasionally tens of hours (Sasson Bitters et al., 2022). This is not sufficient to understand the long-term catalyst degradation that occurs after extended coking. To simulate the effect that long-term exposure to carbonaceous gases would have on varying nickel-to-cobalt ratios, accelerated coking tests were carried out. To maximise the amount of coke-induced degradation in a reasonable time, a relatively low, but still applicable, temperature of 600 ˚C was used. Since the presence of CO_2 in the stream can oxidise and aid coke removal, the accelerated coking tests were carried out in 5% CH_4 in N_2. Accelerated coking tests such as these are commonly applied when running *in-situ* experiments (Weber et al., 2021; Mutz et al., 2018). After four hours on stream under these accelerated coking conditions, each of the catalysts was analysed in order to gain a deeper understanding of how the nickel-to-cobalt ratio affected the type and quantity of the coke formed and the influence these factors had at the catalyst-particle scale.

3.4. Analysis/characterisation of catalysts subjected to accelerated coking tests

3.4.1. Bulk characterisation

After accelerated coking tests, the catalyst samples all appeared black, although their consistency and the apparent tap density of the spent catalyst powders appeared to vary. TGA was performed on each of the catalyst samples to determine the quantity of carbon and gain information about its type and how this varied with nickel-to-cobalt ratio. The results from the TGA testing are shown in Fig. 4. Fig. 4(a) shows the percentage weight change against the temperature for each of the samples. Based on these results it was possible to infer the quantity of carbon formed on each of the samples (see insert Fig. 4(a)). As expected from previous studies (Li et al., 2021), the 20Ni sample contains the largest

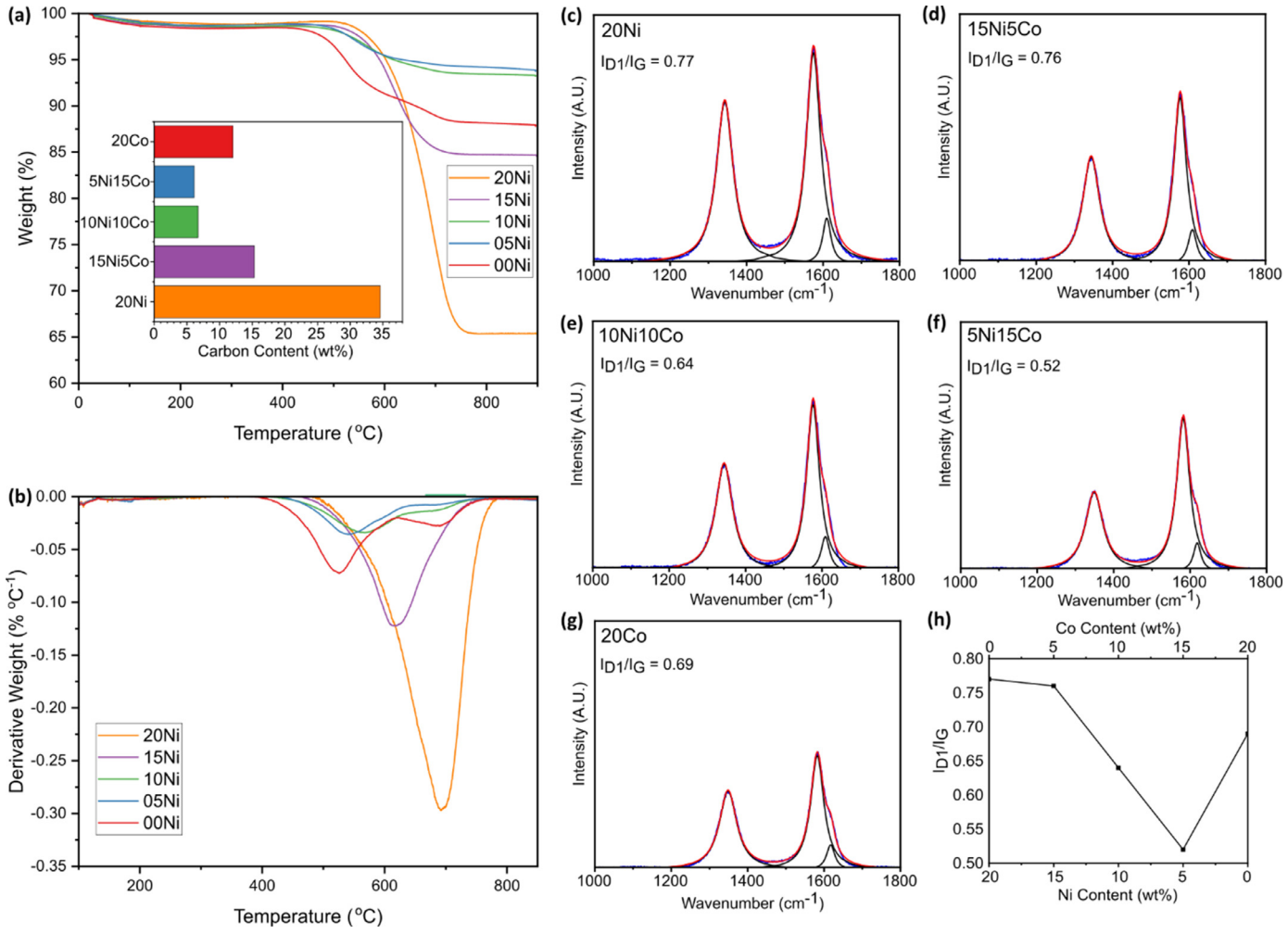

Fig. 4. (a) TGA curves of all coked catalyst samples with their wt% carbon content (inlay) and (b) their differential weight change. Raman spectra of the coked catalysts for (c) 20Ni; (d) 15Ni5Co; (e) 10Ni10Co; (f) 5Ni15Co; g) 20Co. Acquired data shown in blue, fitted data shown in red, and deconvolution in black. (h) Variation of I_{D1}/I_G quotient as a function of nickel-to-cobalt ratio.

quantity of carbon with a weight loss of 35 wt%. Due to the higher quantity of nickel present in this sample it is likely that more of the $NiAl_2O_4$ spinel phase is present. Despite this, the significant quantities of metallic nickel present in the sample from the reduced NiO results in significant quantities of coke formation. Alteration of the preparation methods to produce more of the spinel phase would likely improve the resistance of this catalyst to coking. The addition of Co to give the 15Ni5Co sample had a significant impact on the quantity of carbon formed with the carbon content dropping to 15 wt%. Addition of further cobalt to give the 10Ni10Co sample further improved the coke resistance of the catalyst with carbon content dropping to 7 wt% and the 5Ni15Co sample carbon content was found to be less at *ca.* 6 wt%, however by this point it appears that the improvements were diminishing. Interestingly, when the nickel is removed to give the 20Co sample, there was an increase in coke formation (*ca.* 12 wt%), illustrating the benefits of bimetallic catalysts, whereby the synergistic effects of combining two metals results in properties not observed for either of the metals alone.

The derivative weight change is shown in Fig. 4(b), the positions of the peaks in this plot indicate the temperatures at which the majority of the carbon is removed from the bulk catalyst. If the type and composition of the carbon were consistent across all samples, the temperature at which the carbon burnt off would be expected to be the same, barring any small catalytic effects of the metals present. Based on the results shown in Fig. 4(b), the type of carbon formed was dependant upon the nickel-to-cobalt ratio present in each sample.

For the 20Ni sample, most carbon was removed at *ca.* 700 °C, higher than the other samples, and this relatively high temperature could be interpreted as there being more graphitic carbon present in this sample, since graphitic carbon tends to be more thermally stable than amorphous carbon. With the addition of small quantities of cobalt to produce the 15Ni5Co sample, the peak position moved to a lower temperature of *ca.* 600 °C, indicating that the type of carbon is different in this sample relative to the 20Ni, as the coke formed is less thermally stable. Addition of more cobalt to form the 10Ni10Co and 5Ni10Co samples further changed the peak position and shape, although these two samples did appear similar to one another. For these two catalysts, two small peaks were present at *ca.* 700 °C, which indicate that there was a small quantity of carbon present with a similar thermal stability to that seen in the 20Ni sample, but the majority was composed of carbon that decomposes at *ca.* 550 °C.

Finally, the 20Co sample showed peaks similar to the high-cobalt-containing mixed catalysts with peaks present at both 700 °C, similar to 20Ni, but the 20Co also had a major peak at just below 550 °C, indicating the majority of the carbon present was in the less thermally stable form. These results show the significant effect that the nickel-to-cobalt ratio has on the quantity and type of carbon formed during operation.

Raman spectroscopy was performed on each of the coked catalyst samples to provide bulk characterisation of the formed carbon. Two major peaks associated with the D and G band of carbon were observed in the 1000–1800 cm^{-1} range. The Raman spectra obtained in this wavenumber range for each of the catalysts is shown in Fig. 4(c) – (g). According to work by Sadezky et al., the first-order region of the Raman spectra can be deconvoluted and fitted to five bands; four Lorentzian-shaped bands at 1580, 1350, 1620 and 1200 cm^{-1} referred to G, D1, D2 and D4, respectively, and one Gaussian-shaped band at 1500 cm^{-1}, referred to as D3 (Sadezky et al., 2005). The G band is commonly referred to as the graphitic band and corresponds to an ideal graphitic lattice vibration mode. As such, the ratio of this peak to the D1 peak is often used to give an indication of how disordered or graphitic a carbonaceous material is. While these two bands are regularly used, it is less common to investigate the D2, D3 and D4 bands. The D3 band is likely related to the amorphous sp^2-bonded forms of carbon such as those present in polycyclic aromatic compounds or other organic molecules and fragments. The D4 band can likely be attributed to sp^2-sp (Jang et al., 2019) bonds or C–C and C = C stretching vibrations of polyene-like structure (Sadezky et al., 2005).

From the results shown in Fig. 4(c) - (g), it may appear that all catalyst samples give similar Raman spectra, however, when deconvoluted to give the five bands discussed, information on the differing nature of the carbon can be obtained. The ratio of the intensity of the D1 band to G band gives an indication of the ratio of the disordered carbon to the carbon that is graphitic in nature. Based on the acquired data, the 20Ni catalyst had the highest quantity of disordered carbon present. This apparent discrepancy with the TGA data is addressed in the next section. Addition of a small quantity of cobalt resulted in a decrease in the I_{D1}/I_G ratio, suggesting more graphitic carbon was formed for this sample. (Fig. 4(h)) Further addition of cobalt to form the 10Ni10Co and 5Ni15Co samples both resulted in a decrease in I_{D1}/I_G, suggesting that the more cobalt that there is in the system, the higher the degree of graphitic carbon formation. While the addition of increasing quantities of cobalt caused I_{D1}/I_G to continuously decrease, when nickel was removed completely (20Co sample), the I_{D1}/I_G value increased. This again illustrates the beneficial nature of bimetallic catalysts possessing properties that neither metal possesses alone.

For all nickel-to-cobalt ratios, bands representing graphitic carbon (G) and defects/heteroatoms present in graphitic lattices (D1 and D2) were observed, however there were no D3 and D4 bands present. The D3 and D4 bands are related to the sp (Bauer et al., 2022) and sp (Jang et al., 2019) hybridised carbons found in typical carbon chains, *e.g.*, polyene C–C and C=C type bonds, suggesting that there were few of these forms of carbon present within the coked catalyst samples, implying that the carbon formed was almost purely graphitic in nature, but with varying amounts of defects present.

XRD of the coked samples (Figs. S9–13) indicated that after accelerated coking studies there was little change to the crystallographic nature of the catalysts observable using this technique. The majority of the metals remained present in their reduced form with small amounts of NiO reformed in the high nickel containing catalysts and a small additional peak ascribed to the formed coke was observed. The exception to this was the 20Ni system where larger NiO peaks were observed in addition to the metallic nickel peaks, it is not clear why this sample shows oxidation while others do not, all samples were treated in the same manner, but it is possible that this oxidation may be related to the significant morphological changes that occurred to this sample which are discussed in more detail below.

3.4.2. SEM and TEM analysis

To understand how the nickel-to-cobalt ratio influences the extent and type of coking of these catalyst systems, methods other than bulk analysis techniques are required. The ratio of metals not only affects the quantity and properties of the coke formed as analysed in Section 3.4.1 but can also have a significant effect on the catalyst-support particle as whole. SEM micrographs of the coked samples are shown in Fig. 5(a) – (f). Comparison of these images with those of the reduced catalysts shown in Fig. 3 show that a significant change in morphology has occurred during the accelerated coking procedure. In addition to this, while the reduced catalyst particles all appeared relatively similar, there was a significant difference between the coked samples based on the composition of the catalyst, indicating that nickel-to-cobalt ratio has a significant influence on the resulting morphology.

The 20Ni catalyst was distinctly different from its reduced form, with individual catalyst particles no longer visible - these were replaced with long elongated forms with a texture significantly different to that of the original catalyst particles. Based on the image shown in Fig. 5(a), it appears as though the particles were entirely coated or consisted almost entirely of fibrous carbon. A similar, albeit less drastic, effect was observed for the 15Ni5Co catalyst sample shown in Fig. 5(b). Here the elongated forms did not appear as long and some of the rough catalyst-support particle shape observed in the reduced sample was retained. This image appears to show plates of the support connected by fibrous carbon, consistent with carbon having formed within particles, cracking them apart. Interestingly, all cracks appeared parallel as if delamination had occurred along the same crystallographic plane. The 10Ni10Co and 5Ni15Co samples shown in Fig. 5(c) and (d) most closely resembled that of the reduced catalysts prior to coking. The catalyst particles were clearly visible with little change in shape or size, although they did appear to have some fibrous, carbonaceous species formed on the surface.

The 20Co sample was distinctly different to both the 20Ni and the bimetallic catalysts (Fig. 5(e) and (f) (magnified)). The formation of fibrous carbon across the surface of catalyst particles was observed and while the particles retained their rough shape, significant cracks were evident. These cracked particles, however, appeared significantly different from the cracks observed for the other systems.

Fig. 5(g) - (j) shows TEM micrographs of the coked catalysts. TEM analysis confirms the presence of filamentous carbon. This form of carbon is thought to form through the following mechanism. First, carbon is absorbed on the surface of metal particles giving C_a. Most of this carbon is gasified, first methane dissociates on the surface of metallic nickel producing reactive carbon species, often referred to as alpha carbon, C_a. Most of this form of carbon is gasified but a small proportion is converted into the beta form, C_b, a less reactive form which either begins to encapsulate the active nickel or dissolves into the nickel itself (Trimm, 1997). Dissolution of carbon into the nickel structure can result in the formation of carbon whiskers. The dissolved carbon tends to dissolve through the nickel particle to the rear of the crystallite, where the carbon begins to precipitate, such that continuous build-up results in the formation of carbon whiskers which break the nickel particle from the surface of the support (Trimm, 1997). While this type of carbon formation is often seen as less severe than other forms of coke which coat the active surface and deactivate the catalyst, excessive formation of this type of carbon has been shown to destroy catalyst particles or block the reactor (Liu et al., 2011). The dark particles observed in Fig. 5(g) – (j) are thought to be metal particles and their presence in all samples supports this universal mechanism of filament/ whisker formation. The formation of carbon whiskers in this manner has previously been deemed responsible for the fragmentation of catalyst particles (Ochoa et al., 2020), as is clearly observed in the case of 20Ni, 15Ni5Co and 20Co samples. The extent of cracking appears to be related to the quantity of carbon formed since the 20Ni sample, which had the largest amount of carbon present after testing, resulted in the most significant particle breakdown, followed by the 15Ni5Co catalyst which has the second highest quantity of carbon present.

Despite all systems showing the presence of this filamentous carbon, there are differences between the samples, with the nickel-to-cobalt ratio appearing to have an influence and effect on the morphology. One of the main differences between the 20Ni and the other samples is the presence of small particles of support intertwined with the carbon filaments. This suggests a more significant break-up of the support in this sample

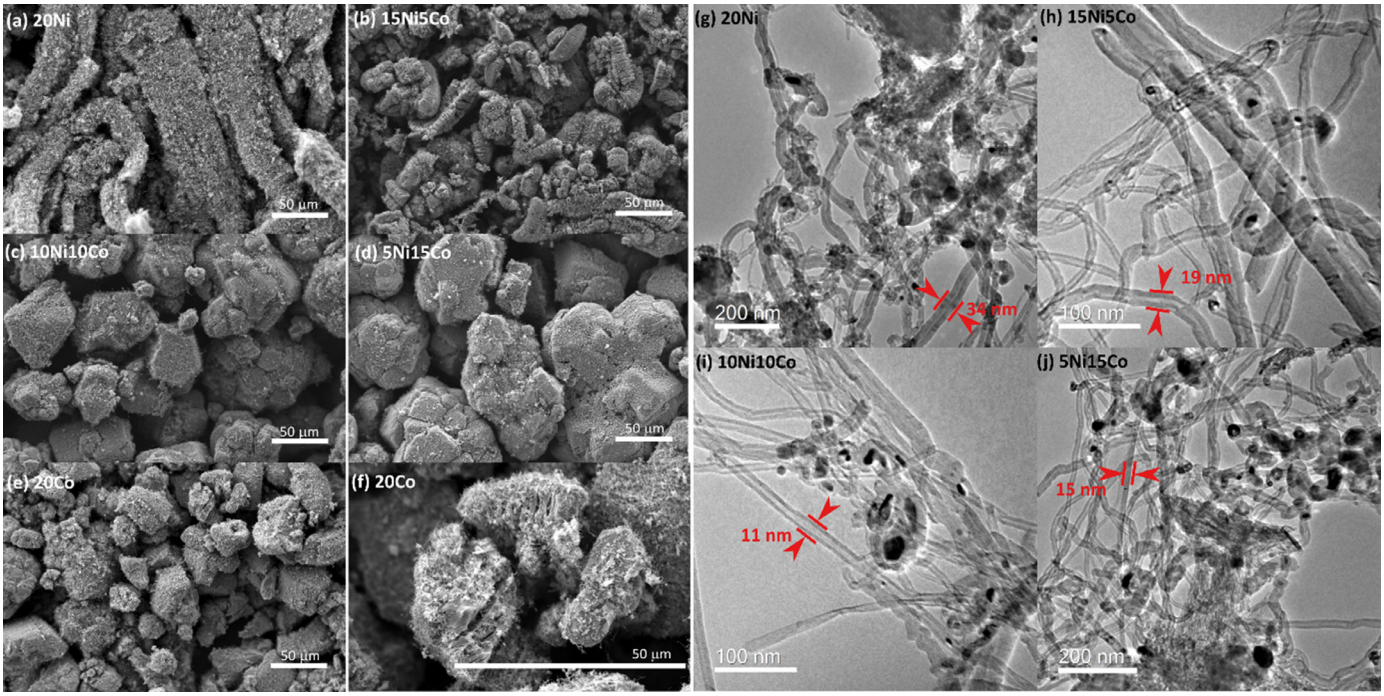

Fig. 5. SEM and TEM micrographs of the catalyst particles post-coking, displaying the morphology of the carbon formed. (a-e) show representative SEM micrographs for the coked 20Ni, 15Ni5Co, 10Ni10Co, 5Ni15Co and 20Co samples, respectively. A higher magnification SEM micrograph of a 20Co catalyst particle is shown in (f). Representative TEM micrographs for 20 Ni, 15Ni5Co, 10Ni10Co and 5Ni15Co samples are shown in (g-j), respectively.

than all of those containing cobalt. In addition to the presence of small support fragments, there are significant differences in the thickness of the carbon filaments. For the 20Ni sample, it mainly consisted of relatively thick, multi-walled, carbon filaments, predominantly *ca.* 40 nm in diameter with a wall thickness of *ca.* 17 nm. For the 15Ni5Co sample, there were still some of these larger thicker-walled filaments but in addition there were also numerous thinner filaments with a diameter of *ca.* 20 nm and wall thickness of *ca.* 5 nm. When the cobalt loading is increased (10Ni10Co), no larger, thicker filaments are present with most filaments measuring *ca.* 15 nm in width, with wall thickness of *ca.* 5 nm. The 5Ni15Co sample consisted almost entirely of filaments in the 15–20 nm range with a wall thickness of approximately 5 nm.

The TEM micrographs support the Raman spectroscopy and TGA data presented in Fig. 4. As the cobalt content is increased, the I_{D1}/I_G ratio decreases, suggesting an increase in the graphitic nature of the carbon present in the sample. Consequently, it would be expected that the temperature at which the carbon is thermally degraded and removed would increase, however for these samples the opposite is true. Bimetallic samples with increasing cobalt content combust at lower temperatures, which would typically be expected for samples with higher I_D/I_G ratios. This apparent contradiction is explained by the carbon morphology. Studies have shown that carbon nanotubes (CNTs) with larger diameters and thicker walls will thermally decompose at higher temperatures than narrower CNTs. (Singh et al., 2010) In addition to increased thermal stability, a more prominent D-band is observed in their Raman spectra due to the more defective nature of thick, multi-walled CNTs, resulting in higher I_{D1}/I_G ratios for larger, thicker-walled CNTs (Singh et al., 2010). There are two main peaks present in the derivate weight change TGA plot (Fig. 4(b)), one at *ca.* 700 °C and another at *ca.* 550 °C. It is likely that the peak at 700 °C relates to the thicker-walled, 40-nm-diameter filaments, whereas the peak at *ca.* 550 °C corresponds to the narrower CNTs observed with diameters in the range 15–20 nm. This would be consistent with the fact that the 20Ni sample has almost exclusively thick CNTs, and has a prominent peak at 700 °C, whereas the bimetallic catalysts have peaks covering both types. The 10Ni10Co and 5Ni15Co samples, which are composed almost exclusively of the thinner type of filament possess only a very small peak at 700 °C, with a far more prominent peak present at 550 °C. The decreasing I_D/I_G ratio in the bimetallic catalysts with increasing cobalt supports the formation of thinner filaments.

3.4.3. *X-ray nano-CT*

Accessible, lab-based X-ray nano-CT provided three-dimensional information about the catalyst samples both post-reduction and post-coking. Raw ortho-slices, segmented ortho-slices, full volume renderings, and volume renderings of "internal non-support" phase of sub-volumes are shown for the as-reduced samples in Fig. 6, and similarly for the samples post-coking in Fig. 7. It should be noted that "internal non-support" phase relates to the darker grayscale regions, internal to the catalyst support particles which are either macropores (in the case of as-reduced samples) or a combination of macropores *and* carbonaceous material (in the case of as-coked samples), to a greater or less degree. The carbonaceous filaments are not sufficiently large or X-ray attenuating to be detected here.

Figs. S14-19 show several slices from various sections of each sample. It is clear from Fig. 6(a) – (c) that there were interparticle voids present within all as-reduced samples, prior to exposure to CH_4 at elevated temperatures, as well as macroporosity within individual support particles; the tomograms showed that the samples prior to coking were nominally the same in this regard. It is worth noting that since the spatial resolution of this technique has been estimated to be between 320 and 740 nm, the meso- and micropores known to be present within the Al_2O_3 support particles are not resolved in this study, although the largest of these may be resolvable by synchrotron X-ray ptychographic techniques (Weber et al., 2022). Some 'excess' large metal particles were observed on the support particle surfaces but this is not thought to majorly influence the behaviour of samples in this study given that the size of these particles (indeed, observable by X-ray CT) is significantly

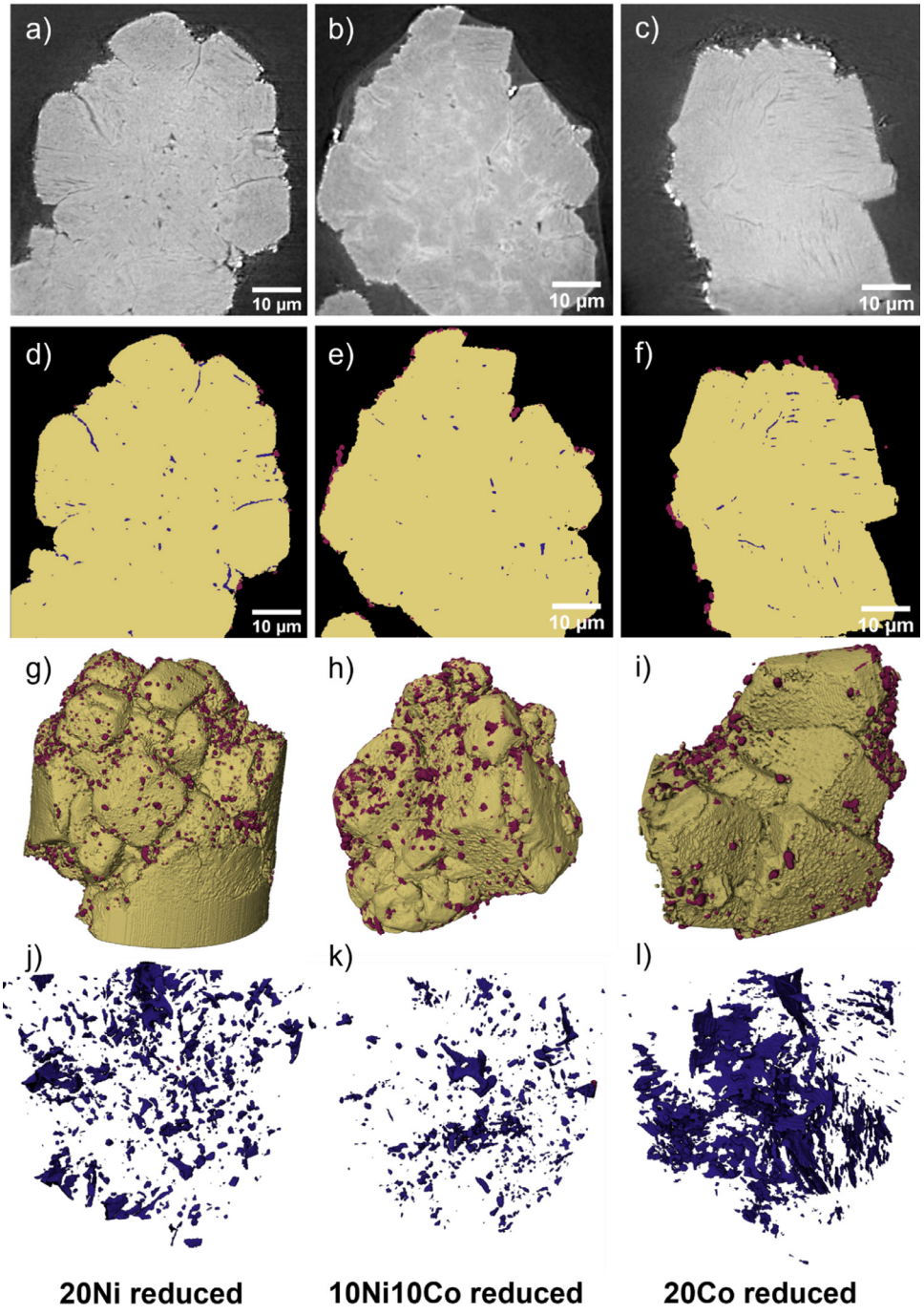

Fig. 6. X-ray nano-CT of as-reduced samples: (a)-(c) Raw ortho-slices in three orthogonal directions; (d)-(f) Segmented ortho-slices thereof; (g)-(i) Full sample volume renderings; (j)-(l) Internal non-support phase volume renderings of sample sub-volumes. Left-hand column for 20Ni; middle column for 10Ni10Co and right-hand column for 20Co. Yellow signifies supported catalyst, purple signifies metal, black signifies air, blue signifies internal non-support phase.

larger than the catalytically active particles contained within the catalyst support particles. This demonstrates the power of lab-based X-ray CT for identification of large metal particles, something that is not easily achieved with the majority of other techniques normally employed for heterogenous catalyst characterisation. None of these larger metal particles are observed within the support particle. Based on these observations it might be expected that there may be a gradient from the centre of the support particle to the surface in terms of metal concentration, however based on the cross-sectional SEM-EDX shown in Fig. 2, this gradient is not significant. Fig. 6(d) – (f) represent robust segmentations of air (black), yellow (supported catalyst), blue (internal non-support) and purple (residual metal) using a machine-learning-based approach, whilst the volume renderings in Fig. 6(g) – (i) display the similar morphology of each of the samples examined, constituting multiple individual support particles adjoined to one another. Fig. 6(j) – (l) illustrate a similar quantity of internal non-support phase associated with a sub-volume (*ca.* 6600 µm^3) extracted from within each sample. A semi-quantitative approach has been taken to characterise the change in morphology associated with the extent of coking observed for each sample. The volume of "internal non-support phase", which encompasses interparticle voids and macropores, as well as undetectable carbonaceous material, has been estimated by voxel counting after segmentation. It should be reiterated that features below the resolution limit will not be detected and therefore are excluded from this analysis. Table 4 illustrates that this phase constituted approximately 0.4–1.4% across the as-reduced samples, supporting the assertion that these samples were nominally the same in terms of interparticle voids and macropores.

As observed from the two-dimensional SEM imaging, the morphology is significantly changed following the accelerated coking procedure, and vast differences between samples are apparent, as seen in Fig. 7.

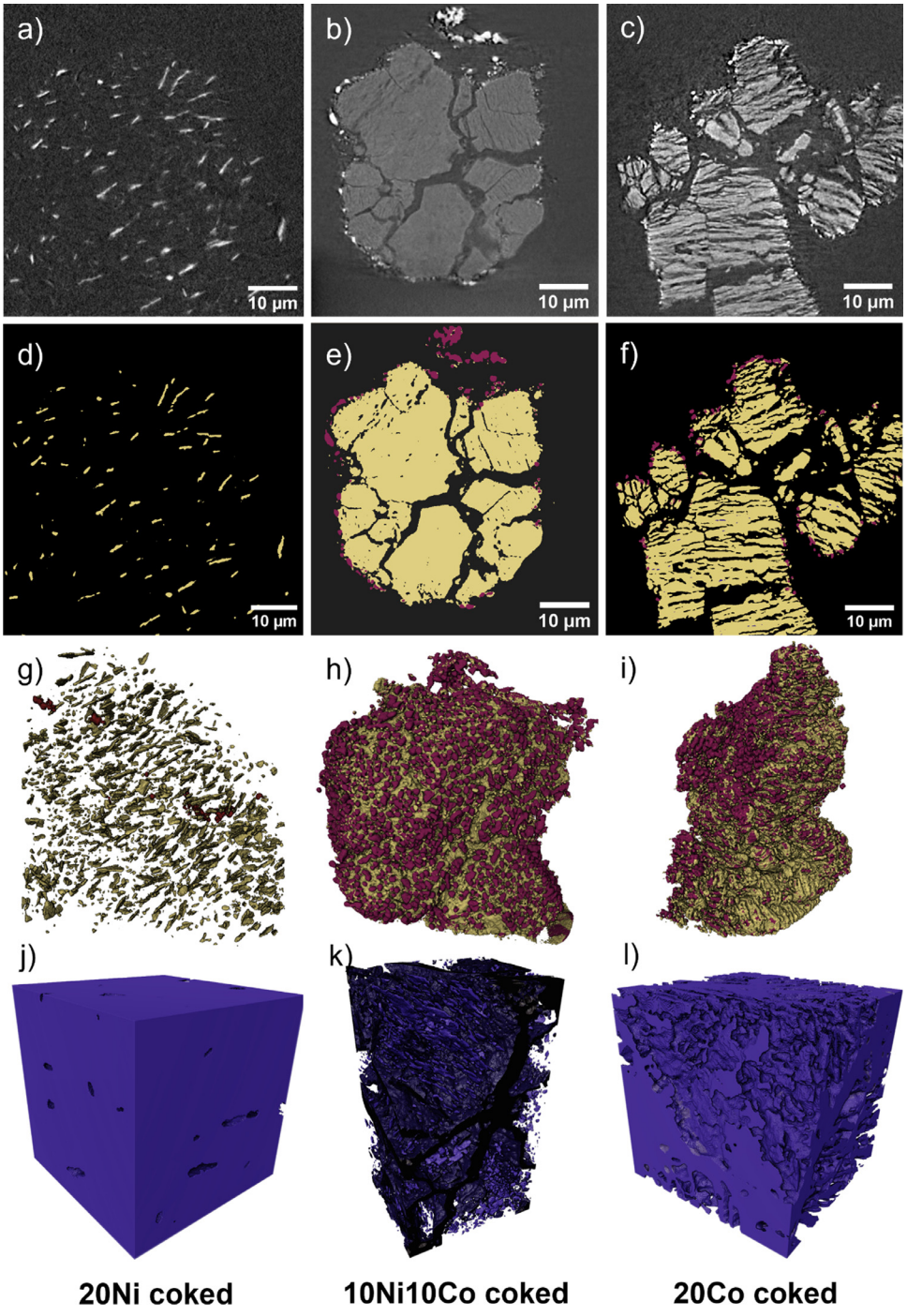

Fig. 7. X-ray nano-CT of coked samples: (a)-(c) Raw ortho-slices in three orthogonal directions; (d)-(f) Segmented ortho-slices thereof;; (g)-(i) Full sample volume renderings; (j)-(l) Internal non-support phase volume renderings of sample sub-volumes. Left-hand column for 20Ni; middle column for 10Ni10Co and right-hand column for 20Co. Yellow signifies supported catalyst, purple signifies metal, black signifies inter-particle voids, blue signifies internal non-support phase.

Table 4
Internal non-support phase fraction for 20Ni, 10Ni10Co and 20Co samples based on voxel counting of segmented sub-volumes.

Sample	As-reduced Internal non-support phase	As-coked
20Ni	1.0%	97.7%
10Ni10Co	0.4%	24.8%
20Co	1.4%	51.9%

Firstly, the most significant morphological change can be seen to occur in the 20Ni sample, as observed in 2D in the SEM micrograph of Fig. 5(a). At first viewing, the foreground material appears counterintuitively to be unconnected and therefore floating in the air, however this apparent discrepancy is explained by the low X-ray attenuation coefficient of the carbonaceous material that surrounds the broken shards of the support. It is supposed that coking has occurred to such a significant degree that the bulk of the imaged sample is in fact carbon, but the contrast *versus* air is insufficient to detect all three phases. It is evident that the original support structure is no longer present, and the vast majority of the remaining sample comprises carbon material that is not directly observed using the X-ray CT technique, both due to the technique's resolution and the low density of the carbon material. Fig. 6(a) – (c) shows that there are some parallel cracks within particles, as inferred from the SEM micrographs shown in Fig. 1 (highlighted by red arrows). It is thought that these represent weak points that help explain the morphology of the coked samples wherein parallel shards of alumina support appear interspersed within carbonaceous

filament networks. A sub-volume within the sample, delimited by the visible fragments, was extracted and the blue volume shown in Fig. 7(j) represents "internal non-support phase", comprising both previous and newly formed voids but mostly filamentous carbon, all ascribed to this one composite phase as the carbon phase is not distinguishable. Clearly, a vast reduction in the volume percentage attributable to supported catalyst and excess metal was observed, which is quantified in Table 4. The next most significant transformation occurred in the pure cobalt sample (20Co). Fig. 7(f) clearly displays that coking has led to significant breakdown of the individual support particles and their cracks can be seen to align with one another, potentially along a single crystallographic direction. Although the support particle structure has degraded, the overall morphology is intact, highlighting that the behaviour of 20Co differs from that of 20Ni, and the lesser degree of coking (corroborated by TGA) leads to less support particle degradation in the former. This is also consistent with the observations by SEM of parallel cracking within catalyst support particles (Fig. 5(f)).

However, the morphological change in the 10Ni10Co catalyst is clearly less dramatic still. Although not observable from two-dimensional SEM, some minor internal cracking between previously adjoined catalyst support particles was evident from the X-ray tomograms of this sample (see Fig. 7(b)). On the other hand, far fewer cracks were present within each individual catalyst-support particle, indicating a different degradation pathway from that followed by 20Co (and indeed 20Ni). Consistent with the lesser extent and different nature of the coking indicated by TGA and Raman spectroscopic analysis, the bimetallic catalyst (10Ni10Co) appeared more resistant to the accelerated coking procedure used in this study than the individual metals, exhibiting greater morphological durability and therefore suitability for this important industrial process. For the 10Ni10Co and 20Co samples, wherein the support particle morphology is broadly retained, there is a significant increase in the presence of large metal particles on the exterior surface of the catalyst-support particles. When compared to the as-reduced samples in Fig. 6, the significant extent of this agglomeration can be seen. This shows the power of X-ray CT for not only tracking the breakdown of catalyst particle structures but also for the study of the spatial redistribution of metals during coking, something that is not possible with the techniques regularly used for catalyst characterisation. This metal redistribution is significant since the formation of these large metal particles must result in the loss of the smaller, high-activity particles, below the resolution of the X-ray CT, meaning a loss in catalyst performance. It is thought that this phenomenon is not only related to the high temperatures that the catalysts have been subjected to but also due to the atmosphere the catalyst is exposed to. All as-reduced catalysts shown in Fig. 6 were subjected to higher temperatures (750 °C) than those during the accelerated coking (600 °C), as such the agglomeration behaviour is likely related to the presence of methane. Further time-resolved 4D tomography is planned to investigate this effect.

By extraction of a similarly sized sub-volume from each of the six samples investigated, simple voxel counting of the phases attributed to solids (supported catalyst and excess metal) and internal non-support phase (*i.e.*, voids and filamentous carbon) was performed and the results are shown in Table 4. The quantification is consistent with the above qualitative analysis: the largest "internal non-support phase" increase, thought to be mostly carbon, was observed to occur for the 20Ni sample, and least for the bimetallic case (10Ni10Co), whilst the pure cobalt (20Co) case displays intermediate behaviour. Volume renderings of the segmented phase that does not contain support or catalyst are shown in Fig. 7 (j-l), with the internal non-support phase for the 10Ni10Co case shown in black, indicating the lower degree of intra-particle cracking (blue) present in this sample, *versus* the 20Co sample.

This sort of particle degradation can have a significant impact on catalyst performance, potentially leading to reactor blockage but just as significantly, it may impede catalyst reactivation. Coking is a common occurrence in hetero-catalytic processes where carbon is involved. In many cases, catalysts can be reactivated relatively easily by oxidising carbon deposits, removing them in the form of carbon dioxide and re-exposing the coated catalyst surfaces. Due to the lower thermal stability of the filamentous carbon, it is often seen as a less serious form of coking since it can be more easily removed at lower temperatures and is less prone to coating active layers. Here, however, the serious implications of the filamentous carbon formation are demonstrated. Should the 20Ni catalyst be reactivated by the removal of carbon the remaining support particles are so deleteriously affects that the regenerated catalyst would retain none of its mechanical strength and cause serious issues with reactor performance. The introduction of cobalt to the system (*e.g.*, 10Ni10Co) aids the reduction of coke formation resulting in a catalyst that would retain some mechanical strength after regeneration or would have to be regenerated significantly less often, improving process efficiency.

The X-ray nano-CT results shown here clearly corroborate the findings from the other characterisation performed as part of this study, but also give rise to extra insights with respect to the types and extent of cracking occurring in the samples with different nickel-to-cobalt ratios. Moreover, X-ray nano-CT has been shown to be a robust tool for quantifying the extent of support degradation by quantifying the "porosity" changes as a function of the nickel-to-cobalt ratio, indicating once more than the synergy between Ni and Co gives rise to a more robust supported catalyst than either of the monometallic analogues. In addition to these important insights into support particle behaviour, the technique has been used to clearly show agglomeration issues that are occurring during the accelerated coking tests that would have significant impact on the catalyst performance. The spatially resolved nature of X-ray CT means that this technique can give vital information to understand catalyst deactivation that is not clearly obtained from any of the other techniques employed.

4. Conclusions

The use of bimetallic catalysts has been shown to have a significant impact on the performance of catalyst systems for the dry reforming of methane, whereby dual metal systems result in behaviour not observed in either of the single metal systems. The nickel-to-cobalt ratio in the bimetallic system has a considerable influence on both the quantity and properties of carbon formed during accelerated coking.

The system containing only nickel was observed to result in the largest quantity of carbon formation with the introduction of cobalt significantly reducing the extent of coking. For the bimetallic systems, a nickel-to-cobalt ratio of 10Ni10Co or 5Ni10Co was observed to be optimal in terms of coking resistance. An increased quantity of cobalt also resulted in the formation of less thermally stable carbon fibres.

Lab-based X-ray nano-computed tomography was used effectively to show that it is not only the quantity and bulk properties of the deposited carbon that are important. To gain a deeper understanding of coke formation and ensure long catalyst lifetimes, it is important to consider phenomena occurring at the scale of the supported catalyst particles. Both the nickel- and cobalt-only samples showed significant and detrimental supported catalyst particle cracking that is not observed in the mixed 10Ni10Co system. Interestingly, the technique also provides insights into agglomeration of active metal particles in to large, likely inactive, particles during coking. Further studies are planned to gain a better understanding of this phenomenon since the effect, if any, of nickel-to-cobalt ratio on agglomeration is not clear.

The ease and relatively cheap nature of lab-based X-ray computed tomography measurements opens the possibility of the specially resolved tomographic techniques becoming used in the design and formulation of future catalysts. The nature of the information that can be obtained using these methods is something that is not currently easily available for catalyst designers but, as shown in this work, can give information key to understanding catalyst degradation and methods for overcoming these factors.

Declaration of Competing Interest

The authors declare that they have no known competing financial interests or personal relationships that could have appeared to influence the work reported in this paper.

Acknowledgements

This work was supported by the Qatar National Research Fund (QNRF) from National Priority Research Program (NPRP9–313–2–135) and funding from the Faraday Institution (EP/S003053.1, grant numbers FIRG014 and FIRG015). Use of X-ray CT instruments was supported by the EPSRC (EP/K005030/1 and EP/P009050/1). The Royal Academy of Engineering is acknowledged for funding the Research Chairs of Shearing and Brett (including the National Physical Laboratory and HORIBA MIRA). Steve Hudziak and the CDT-ACM are gratefully acknowledged for their help with the Raman spectroscopy measurements.

Supplementary materials

Supplementary material associated with this article can be found, in the online version, at doi:10.1016/j.ccst.2022.100068.

References

Abdollahifar, M., Haghighi, M., Babaluo, A.A., Talkhoncheh, S.K., 2016. Sono-synthesis and characterization of bimetallic Ni-Co/Al_2O_3-MgO Nanocatalyst: effects of METAL CONTENT ON CATALYTIC Properties and Activity for hydrogen production via CO_2 reforming of CH_4. Ultrason. Sonochem. 31, 173–183.

Bare, S.R., Charochak, M.E., Kelly, S.D., Lai, B., Wang, J., Chen-Wiegart, Y.C.K, 2014. Characterization of a fluidized catalytic cracking catalyst on ensemble and individual particle level by X-Ray Micro- and Nanotomography, Micro-X-Ray fluorescence, and Micro-X-Ray diffraction. ChemCatChem 6 (5), 1427–1437.

Bauer, C., Treyer, K., Antonini, C., Bergerson, J., Gazzani, M., Gencer, E., Gibbins, J., Mazzotti, M., McCoy, S.T., McKenna, R., Pietzcker, R., Ravikumar, A.P., Romano, M.C., Ueckerdt, F., Vente, J., van der Spek, M., 2022. On the climate impacts of blue hydrogen production. Sustain. Energy Fuels 6 (1), 66–75.

Beale, A.M., Jacques, S.D.M., Gibson, E.K., Di Michiel, M., 2014. Progress towards five dimensional diffraction imaging of functional materials under process conditions. Coord. Chem. Rev. 277, 208–223.

Berg, S., Kutra, D., Kroeger, T., Straehle, C.N., Kausler, B.X., Haubold, C., Schiegg, M., Ales, J., Beier, T., Rudy, M., et al., 2019. Ilastik: interactive machine learning for (Bio)Image analysis. Nat. Methods 16 (12), 1226–1232.

Bian, Z., Das, S., Wai, M.H., Hongmanorom, P., Kawi, S., 2017. A review on bimetallic nickel-based catalysts for CO_2 reforming of methane. ChemPhysChem 18 (22), 3117–3134.

Cats, K.H., Andrews, J.C., Stéphan, O., March, K., Karunakaran, C., Meirer, F., De Groot, F.M.F., Weckhuysen, B.M., 2016. Active phase distribution changes within a catalyst particle during Fischer-Tropsch synthesis as revealed by multi-scale microscopy. Catal. Sci. Technol. 6 (12), 4438–4449.

Dasilva, J.C., Mader, K., Holler, M., Haberthür, D., Diaz, A., Guizar-Sicairos, M., Cheng, W.C., Shu, Y., Raabe, J., Menzel, A., Vanbokhoven, J.A., 2015. Assessment of the 3-D pore structure and individual components of preshaped catalyst bodies by X-Ray imaging. ChemCatChem 7 (3), 413–416.

Edwards, J.H., Maitra, A.M., 1995. The chemistry of methane reforming with carbon dioxide and its current and potential applications. Fuel Process. Technol. 42, 269–289.

Erdogan, B., Arbag, H., Yasyerli, N., 2018. SBA-15 supported mesoporous Ni and Co catalysts with high coke resistance for dry reforming of methane. Int. J. Hydrogen Energy 43 (3), 1396–1405.

Gadalla, A.M., Sommer, M.E., 1988. The role of catalyst support on the activity of nickel for reforming methane with CO_2. Chem. Eng. Sci. 44 (12), 2825–2829.

Gambino, M., Veselý, M., Filez, M., Oord, R., Ferreira Sanchez, D., Grolimund, D., Nesterenko, N., Minoux, D., Maquet, M., Meirer, F., Weckhuysen, B.M., 2020. Nickel poisoning of a cracking catalyst unravelled by single-particle X-Ray fluorescence-diffraction-absorption tomography. Angew. Chem. Int. Ed. 59 (10), 3922–3927.

Gražulis, S., Daškevič, A., Merkys, A., Chateigner, D., Lutterotti, L., Quirós, M., Serebryanaya, N.R., Moeck, P., Downs, R.T., Le Bail, A., 2012. Crystallography Open Database (COD): an open-access collection of crystal structures and platform for world-wide collaboration. Nucleic Acids Res. 40 (D1), 420–427.

Han, K., Wang, S., Liu, Q., Wang, F., 2021. Optimizing the Ni/Cu RATIO in Ni-Cu nanoparticle catalysts for methane dry reforming. ACS Appl. Nano Mater. 4 (5), 5340–5348.

He, L., Chen, X., Ren, Y., Yue, B., Tsang, S.C.E., He, H., 2021. Improving catalytic stability and coke resistance of Ni/Al_2O_3 catalysts with Ce promoter for relatively low temperature dry reforming of methane reaction. Chem. Res. Chin. Univ. 1–9.

Jang, W.J., Shim, J.O., Kim, H.M., Yoo, S.Y., Roh, H.S., 2019. A review on dry reforming of methane in aspect of catalytic properties. Catal. Today 324, 15–26.

Kawi, S., Kathiraser, Y., Ni, J., Oemar, U., Li, Z., Saw, E.T., 2015. Progress in synthesis of highly active and stable nickel-based catalysts for carbon dioxide reforming of methane. ChemSusChem 8 (21), 3556–3575.

Kim, D.K., Stöwe, K., Müller, F., Maier, W.F., 2007. Mechanistic study of the unusual catalytic properties of a new Ni-Ce mixed oxide for the CO_2 reforming of methane. J. Catal. 247 (1), 101–111.

Laosiripojana, N., Sutthisripok, W., Assabumrungrat, S., 2005. Synthesis gas production from dry reforming of methane over CeO_2 doped Ni/Al_2O_3: influence of the doping ceria on the resistance toward carbon formation. Chem. Eng. J. 112, 13–22.

Lavoie, J.M., 2014. Review on dry reforming of methane, a potentially more environmentally-friendly approach to the increasing natural gas exploitation. Front. Chem. 2, 1–17.

Li, B., Luo, Y., Li, B., Yuan, X., Wang, X., 2019. Catalytic performance of iron-promoted nickel-based ordered mesoporous alumina FeNiAl catalysts in dry reforming of methane. Fuel Process. Technol. 193, 348–360 January.

Li, B., Yuan, X., Li, L., Wang, X., Li, B., 2021. Stabilizing Ni-Co alloy on bimodal mesoporous alumina to enhance carbon resistance for dry reforming of methane. Ind. Eng. Chem. Res. 60 (47), 16874–16886.

Li, L., Chen, J., Zhang, Y., Sun, J., Zou, G., 2022. Ni-Co bimetallic catalysts on coconut shell activated carbon prepared using solid-phase method for highly efficient dry reforming of methane. Environ. Sci. Pollut. Res., 0123456789.

Liu, C.J., Ye, J., Jiang, J., Pan, Y., 2011. Progresses in the preparation of coke resistant Ni-BASED CATALYST FOR STEAM and CO_2 reforming of methane. ChemCatChem 3 (3), 529–541.

Luisetto, I., Tuti, S., Di Bartolomeo, E., 2012. Co and Ni supported on CeO_2 as selective bimetallic catalyst for dry reforming of methane. Int. J. Hydrogen Energy 37 (21), 15992–15999.

Meirer, F., Weckhuysen, B.M., 2018. Spatial and temporal exploration of heterogeneous catalysts with synchrotron radiation. Nat. Rev. Mater. 3 (9), 324–340.

Meirer, F., Morris, D.T., Kalirai, S., Liu, Y., Andrews, J.C., Weckhuysen, B.M., 2015a. Mapping metals incorporation of a whole single catalyst particle using element specific X-Ray nanotomography. J. Am. Chem. Soc. 137 (1), 102–105.

Meirer, F., Kalirai, S., Morris, D., Soparawalla, S., Liu, Y., Mesu, G., Andrews, J.C., Weckhuysen, B.M., 2015b. Life and death of a single catalytic cracking particle. Sci. Adv. 1 (3), 1–13.

Mutz, B., Sprenger, P., Wang, W., Wang, D., Kleist, W., Grunwaldt, J.D., 2018. Operando raman spectroscopy on CO_2 methanation over alumina-supported Ni, Ni_3Fe and $NiRh_{0.1}$ catalysts: role of carbon formation as possible deactivation pathway. Appl. Catal. A Gen. 556, 160–171.

Ochoa, A.; Bilbao, J.; Gayubo, A.G.; Casta, P. Coke formation and deactivation during catalytic reforming of biomass and waste pyrolysis products : a review. 2020, 119.

Oliveira, A.M., Beswick, R.R., Yan, Y., 2021. A green hydrogen economy for a renewable energy society. Curr. Opin. Chem. Eng. 33, 100701.

Pakhare, D., Spivey, J., 2014. A review of dry CO_2 reforming of methane over noble metal catalysts. Chem. Soc. Rev. R. Soc. Chem. 7813–7837.

Price, S.W.T., Martin, D.J., Parsons, A.D., Sławiński, W.A., Vamvakeros, A., Keylock, S.J., Beale, A.M., Mosselmans, J.F.W., 2017. Chemical imaging of Fischer-Tropsch catalysts under operating conditions. Sci. Adv 3 (3).

Rouibah, K., Barama, A., Benrabaa, R., Guerrero-Caballero, J., Kane, T., Vannier, R.N., Rubbens, A., Löfberg, A., 2017. Dry Reforming of methane on nickel-chrome, nickel-cobalt and nickel-manganese catalysts. Int. J. Hydrogen Energy 42 (50), 29725–29734.

Sadezky, A., Muckenhuber, H., Grothe, H., Niessner, R., Pöschl, U., 2005. Raman microspectroscopy of soot and related carbonaceous materials: spectral analysis and structural information. Carbon N. Y. 43 (8), 1731–1742.

Salhi, N., Boulahouache, A., Petit, C., Kiennemann, A., Rabia, C., 2011. Steam reforming of methane to syngas over $NiAl_2O_4$ spinel catalysts. Int. J. Hydrogen Energy 36 (17), 11433–11439.

Sasson Bitters, J., He, T., Nestler, E., Senanayake, S.D., Chen, J.G., Zhang, C., 2022. Utilizing bimetallic catalysts to mitigate coke formation in dry reforming of methane. J. Energy Chem. 68, 124–142.

Schmidt, J.E., Oord, R., Guo, W., Poplawsky, J.D., Weckhuysen, B.M., 2017. Nanoscale tomography reveals the deactivation of automotive copper-exchanged zeolite catalysts. Nat. Commun. 8 (1), 1666.

Sengupta, S., Ray, K., Deo, G., 2014. Effects of modifying Ni/Al_2O_3 catalyst with cobalt on the reforming of CH_4 with CO_2 and cracking OF CH_4 reactions. Int. J. Hydrogen Energy 39 (22), 11462–11472.

Sharifi, M., Haghighi, M., Rahmani, F., Karimipour, S., 2014. Syngas production via dry reforming of CH_4 over Co- and Cu-promoted Ni/Al_2O_3-ZrO_2 Nanocatalysts Synthesized via sequential impregnation and Sol-Gel methods. J. Nat. Gas Sci. Eng. 21, 993–1004.

Siang, T.J., Singh, S., Omoregbe, O., Bach, L.G., Phuc, N.H.H., Vo, D.V.N., 2018. Hydrogen production from CH_4 dry reforming over bimetallic Ni–Co/Al_2O_3 catalyst. J. Energy Inst. 91 (5), 683–694.

Singh, D.K., Iyer, P.K., Giri, P.K., 2010. Diameter dependence of oxidative stability in multiwalled carbon nanotubes: role of defects and effect of vacuum annealing. J. Appl. Phys. 108 (8).

Sutthiumporn, K., Maneerung, T., Kathiraser, Y., Kawi, S., 2012. CO_2 Dry-reforming of methane over $La_{0.8}Sr_{0.2}Ni_{0.8}M_{0.2}O_3$ perovskite (M = Bi, Co, Cr, Cu, Fe): roles of lattice oxygen on C-H activation and carbon suppression. Int. J. Hydrogen Energy 37 (15), 11195–11207.

Swaan, H.M., Kroll, V.C.H., Martin, G.A., Mirodatos, C., 1994. Deactivation of supported nickel catalysts during the reforming of methane by carbon dioxide. Catal. Today 21, 571–578.

Takanabe, K., Nagaoka, K., Nariai, K., Aika, K.I., 2005. Titania-supported cobalt and nickel bimetallic catalysts for carbon dioxide reforming of methane. J. Catal. 232 (2), 268–275.

Trimm, D.L., 1997. Coke Formation and Minimisation during Steam Reforming Reactions. Catal. Today 37 (3), 233–238.

Tsyganok, A.I., Inaba, M., Tsunoda, T., Uchida, K., Suzuki, K., Takehira, K., Hayakawa, T., 2005. Rational design of Mg-Al mixed oxide-supported bimetallic catalysts for dry reforming of methane. Appl. Catal. A Gen. 292 (1–2), 328–343.

Veselý, M., Valadian, R., Merten Lohse, L., Toepperwien, M., Spiers, K., Garrevoet, J., Vogt, E.T.C., Salditt, T., Weckhuysen, B.M., Meirer, F., 2021. 3-D X-Ray Nanotomography reveals different carbon deposition mechanisms in a single catalyst particle. ChemCatChem 13 (10), 2494–2507.

Weber, S., Diaz, A., Holler, M., Schropp, A., Lyubomirskiy, M., Abel, K.L., Kahnt, M., Jeromin, A., Kulkarni, S., Keller, T.F., Gläser, R., Sheppard, T.L., 2022. Evolution of hierarchically porous nickel alumina catalysts studied by X-Ray ptychography. Adv. Sci. 9 (8), 1–12.

Wang, Y., Yao, L., Wang, S., Mao, D., Hu, C., 2018. Low-temperature catalytic CO_2 dry reforming of methane on Ni-based catalysts: a review. Fuel Process. Technol. 169, 199–206.

Weber, S., Abel, K.L., Zimmermann, R.T., Huang, X., Bremer, J., Rihko-Struckmann, L.K., Batey, D., Cipiccia, S., Titus, J., Poppitz, D., Kübel, C., Sundmacher, K., Gläser, R., Sheppard, T.L., 2020. Porosity and structure of hierarchically porous Ni/Al_2O_3 catalysts for CO_2 methanation. Catalysts 10 (12), 1–22.

Weber, S., Batey, D., Cipiccia, S., Stehle, M., Abel, K.L., Gläser, R., Sheppard, T.L., 2021. Hard X-Ray Nanotomography for 3D analysis of coking in nickel-based catalysts. Angew. Chem. Int. Ed. 60 (40), 21772–21777.

Yentekakis, I.V., Panagiotopoulou, P., Artemakis, G., 2021. A review of recent efforts to promote dry reforming of methane (DRM) to syngas production via bimetallic catalyst formulations. Appl. Catal. B Environ. 296, 120210.

Zhang, Y.S., Lu, X., Owen, R.E., Manos, G., Xu, R., Wang, F.R., Maskell, W.C., Shearing, P.R., Brett, D.J.L., 2020. Fine structural Changes of fluid catalytic catalysts and characterization of coke formed resulting from heavy oil Devolatilization. Appl. Catal. B Environ. 263, 118329.